# History effects on nonwetting fluid residuals during desaturation flow through disordered porous media

Thibaud Chevalier,* Dominique Salin, and Laurent Talon
*Université Paris-Sud, CNRS, Laboratoire FAST, UMR 7608, Orsay F-91405, France*

Andreas G. Yiotis
*Environmental Research Laboratory, NCSR "Demokritos," 15310 Athens, Greece*
(Received 27 January 2015; published 22 April 2015)

We investigate experimentally the sweeping of a nonwetting fluid by a wetting one in a quasi-two-dimensional porous medium consisting of random obstacles. We focus primarily on the resulting phase distributions and the residual nonwetting phase saturation as a function of the normalized wetting fluid flow rate—the capillary number Ca—at steady state. The wetting liquid is then flowing in the medium partially saturated by immobile nonwetting liquid blobs. The decrease of the nonwetting saturation is an irreversible process that depends strongly on flow history and more specifically on the highest value of Ca reached in the past. At lower Ca values, when capillary forces are dominant, the residual steady state saturation depends significantly on the initial phase configuration. However, at higher Ca, the saturation becomes independent of the history and thus follows a master curve that converges to an asymptotic residual value. Blob sizes range over four orders of magnitude in our experimental domain, following a probability distribution function $P$ that scales with the blob size $s$ as $P(s) \propto s^{-2}$ for blob sizes larger than the typical pore size. It also exhibits a maximum size cutoff $s_{\max}$, that decreases as $s_{\max} \propto \mathrm{Ca}^{-1}$. To determine the flow properties, we have measured the pressure drop ($B$) versus the flow rate (Ca). In the ranges of low and high Ca values, the relationship between Ca and $B$ is found to be linear, following Darcy's law ($B \propto \mathrm{Ca}$). In the intermediate regime, the progressive mobilization of blobs leads to a nonlinear dependence $B \propto \mathrm{Ca}^{0.65}$, due to an increase of the available flow paths.

DOI: 10.1103/PhysRevE.91.043015 PACS number(s): 47.56.+r, 47.55.dd, 89.75.Fb

## I. INTRODUCTION

Immiscible two-phase (2P) flow in porous media is a process of significant scientific and technological importance, encountered in a series of environmental and energy-related applications, such as Enhanced Oil Recovery from pressure-depleted petroleum reservoirs, soil remediation from anthropogenic highly toxic pollutants, and carbon dioxide sequestration, among many others.

During immiscible 2P flow processes, several configurations for the phase distributions of the wetting ($w$) and nonwetting ($nw$) fluids are possible depending on flow history, phase saturations, and the capillary number. Of crucial importance for the flow response is the spatial connectivity of each phases, that may or may not span the porous medium [1], and particularly the existence of disconnected $nw$ liquid droplets. The latter configuration is typically encountered at the later stages of imbibition displacement processes, where a medium initially saturated by a $nw$ fluid is flooded with a wetting one.

As the $w$-phase saturation increases, the $nw$ phase becomes progressively disconnected and forms fluid blobs, otherwise called droplets or ganglia [2]. Depending on the capillary number of the flow, two kinds of populations may coexist. The mobile blobs are swept by the $w$ phase, whereas the stranded blobs in weak flow regions reduce the effective medium permeability. The sweep efficiency of the imbibition process significantly depends on the porous medium heterogeneities, where the formation of preferential pathways may bypass the trapped blobs. The recovery of such residuals, that may account for a significant volume fraction of the total storage capacity of the soil formation, is a rather challenging task. Indeed, mobilizing the trapped blobs may require a significant pressure drop and energy consumption.

Several classical experimental and theoretical studies of immiscible 2P flow have focused on the conditions of blob trapping and mobilization in porous domains, such as in pore networks [3–6], model porous media [7,8], and bead-sand packings [9]. Other works have also explored the interaction between mobile and immobile blob populations and classified the flow regimes [2,10]. It offers valuable insight on the effects of flow conditions and flow history on interfacial stability [11] and on the conditions of blob breakup and coalescence [12–15]. A series of more recent studies have focused on effective permeabilities at various flow conditions and $nw$-phase saturations, based on pore scale experiments [16–20], theoretical considerations [16,21], and direct numerical simulations [22]. Such studies have highlighted the effects of blob populations on nonlinear flow regimes, through blocking flow paths and excluding them from the flow stream.

Motivated by such results, we performed an extensive experimental study of immiscible displacement of $nw$-phase residuals by an imbibing liquid within a model porous medium that consists of a two-dimensional transparent Hele-Shaw type cell with solid patches as flow obstacles. The inner walls of the cell were microengineered according to a random field pattern in order to produce flow obstacles which mimic contact areas of a fractured rock sample. This experimental approach allows for the direct monitoring of the blob sizes, shapes and mobility during the process. In the present paper,

*Corresponding author: chevalier@fast.u-psud.fr

 

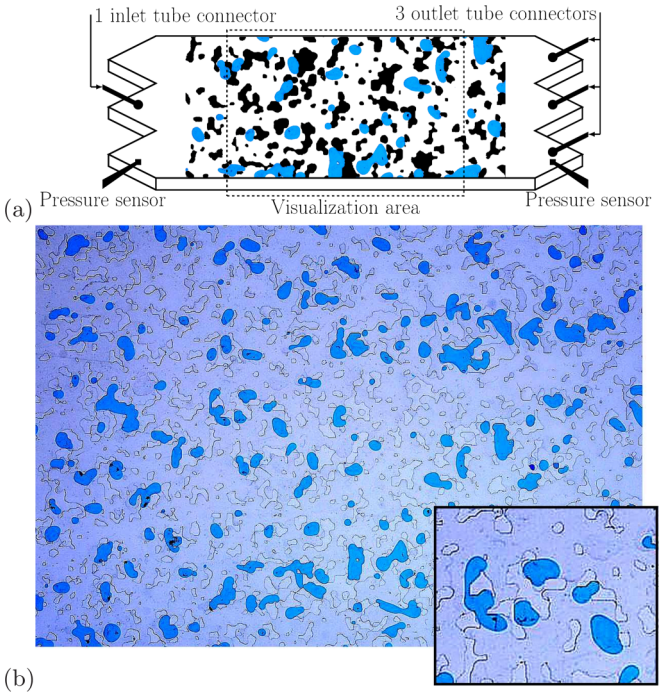


FIG. 1. (Color online) (a) Schematic of the experimental setup of our study that shows the microengineered porous domain and the flow inlet and outlets. (b) Typical snapshot (closeup of size 120 mm × 80 mm) of the porous medium saturated with both phases at steady state. In the enlarged closeup, we can distiguish the stranded nonwetting phase blobs (blue-dyed water), the continuous wetting phase (heptane with light blue color), and the solid obstacles of random shape and size that appear as transparent isolated patches.

we focus on steady-state configurations, where the wetting liquid is flowing through porous medium partially saturated by immobile nonwetting liquid blobs. The main control parameter is the capillary number, Ca, which represents the normalized wetting fluid flow rate. Our experimental setup is able to cover a rather large range of Ca values (over three orders of magnitude) and blob sizes, allowing thus for the study of flow history effects, the identification of different flow regimes, and the calculation of the blob size probability distribution function (PDF).

## II. EXPERIMENTAL SETUP AND PROCEDURE

The porous domain is constructed by gluing together two transparent PMMA [poly(methyl methacrylate)] plates $l = 325$ mm long and $b = 120$ mm wide. The bottom plate is engraved using a computerized milling machine following a stochastically generated pattern (see [22]). This produces obstacles of random size and shape with typical correlation length of 900 $\mu$m. The distance between the two surfaces is $e = 300$ $\mu$m and the porosity is equal to $\Phi = 0.82$. A V-shaped region is also engraved below the flow inlet in order to better homogenize the mixing of the two phases in this transient zone. Thus the porous medium is a kind of Hele-Shaw cell (two parallel plates separated by a small gap $e$) with solid patches (flow obstacles) as shown in the sketch of Fig. 1(a).

The phase distribution patterns are recorded using a digital camera (Nikon $D800$) over a field further downstream in the flow of size 180 mm × 120 mm. The images are then processed in order to compute phase saturations and blob size distributions. The bottom of Fig. 1 is a typical snapshot of the porous medium during a desaturation experiment at steady-state conditions. The water phase (dark blue) is the $nw$ fluid, the oily phase (continuous light blue) is the $w$ fluid, whereas the solid obstacles appear as transparent isolated patches (see also closeup view in the right bottom of Fig. 1). It is worth noting the wide range of obstacle sizes and their rough surface shapes, which provides a significantly different configuration than the single layer of glass beads in a Hele-Shaw cell used in earlier studies [16,17,20,23]. In our system, the typical solid and void sizes range from ∼1 mm up to 30 mm, thus producing a wide distribution of blob sizes, as we will discuss in more detail in the following sections.

*The dry cell is initially fully saturated with the n-heptane w phase.* Both liquids are injected from a single inlet from one side of the cell using one gear pump (Ismatec, 0.1–100 cm$^3$/min) for each fluid. This allows for the fine tuning of the flow ratio of water and oil at the inlet of the medium, leading to a precise control over the mobile saturation ratio at steady state conditions. The liquids exit from three outlets at the downstream end of the cell as shown in Fig. 1.

The permeability $k$ of the medium is measured by performing single phase flow experiments with $n$-heptane while measuring the pressure drop versus the flow rate $Q_w$, leading to $k = \mu Q_w/(b\,e\,|\nabla P|) \approx 2.0 \times 10^{-9}$ m$^2$, where $\mu$ is the dynamic fluid viscosity. The latter can be compared to the Hele-Shaw cell permeability without solid obstacles, $k_{HS} = e^2/12 = 7.5 \times 10^{-9}$ m$^2$, which demonstrates the crucial effect of only 18% of obstacles ($k \sim 0.27 k_{HS}$).

*Experimental procedure.* At the beginning of each experiment, both the $w$ phase ($n$-heptane with viscosity $\mu_w = 4.0 \times 10^{-4}$ Pa s) and the $nw$ phase (blue-dyed water, $\mu_{nw} = 1.0 \times 10^{-3}$ Pa s) are co-injected using two separate gear pumps from a single flow inlet according to a predefined flow ratio $Q_{nw}/Q_w$ in order to achieve a steady-state phase distribution pattern in our domain. The co-injection is achieved by connecting the two fluid pumps to a "Y-shaped" tube where the fluids form a succession of "pearllike" droplets according to the ratio of the pump flow rates. The interfacial tension between the two fluids is $\gamma = 5.2 \times 10^{-2}$ N/m, while we assume that heptane is totally wetting against water in the PMMA medium. We define the capillary number as $\mathrm{Ca} = (\mu_w/\gamma)\, Q_w/(b\,e)$, based on heptane viscosity and velocity, and a dimensionless pressure gradient, $B = e^2|\nabla P|/\gamma$. With the particular set of pumps, we can cover over three orders of magnitude of flow rates, and thus the resulting capillary number ranges from $\mathrm{Ca} = 3.7 \times 10^{-7}$ to $\mathrm{Ca} = 3.7 \times 10^{-4}$. It is worth noting that at the largest flow rate the Reynolds number is $\mathrm{Re} = \rho_w Q_w/(b\mu_w) \sim 20$, where the creeping flow assumption is no longer valid, and we can thus anticipate the onset of inertial effects, as we will discuss in more detail below. We define the $nw$-phase saturation $S$ as the volume ratio of the $nw$ blue fluid over the total fluid.

After sufficient time of fluid co-injection (typically ranging from minutes to a couple of hours), the system eventually reaches a steady state configuration, where both the $nw$-phase saturation $S$ and the pressure drop $B$ remain practically

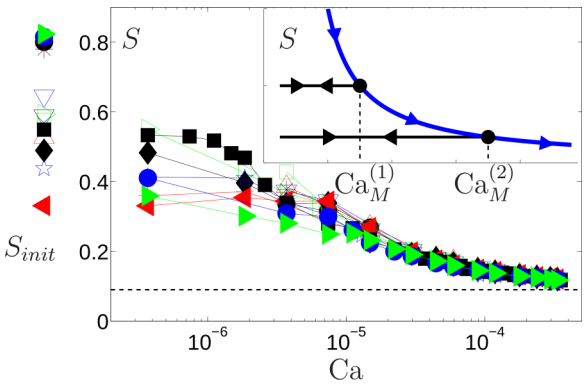


FIG. 2. (Color online) Linear-log plot of the residual saturation of immobile nonwetting fluid $S$ vs the capillary number Ca for different initial conditions (see text). The saturation values on the left side of the vertical axis correspond to the initial nonwetting phase $S_{\text{init}}$ for each experimental series. The inset is a schematic of the desaturation history. The blue curve denotes the "irreversible" branch of the desaturation process, while black curves with double arrows denote "reversible" branches of constant saturation, starting from the historically maximum capillary number values for each "branch" denoted $\text{Ca}_M$.

constant with time. We denote as $S_{\text{init}}$ this steady state $nw$ saturation for the particular flow ratio, that will serve as the initial value for each set of desaturation experiments. This value has been represented by symbols on the left side of the vertical axis of Fig. 2. It is worth noting that the larger the above flow rate ratio, the larger $S_{\text{init}}$.

We then turn off the $nw$-phase injection and continue injecting only the $w$ phase starting from the lowest Ca value. After a sufficient amount of time and for a fixed $w$-phase flow rate, thus Ca, both the pressure drop and the phase distribution patterns eventually reach a new steady state configuration, leading to a new set of constant $S$ and $B$ values. We then gradually increase the $w$-phase flow rate until the system reaches a new steady state. This process is repeated over three orders of magnitude of the capillary number. It is worth noting that for a given Ca, when a constant saturation was achieved, it is possible to decrease Ca without changing $S$ as sketched in the inset of Fig. 2 ("reversible" black branches). This historically maximum capillary number is represented by $\text{Ca}_M$. It allows also the direct measurement of their effective medium permeability at this given saturation. After each set of steady state experiments, we perform a single phase injection of heptane at the maximum flow rate ($\text{Ca} = 3.7 \times 10^{-4}$) to sweep off the effect of the previous set of experiments.

## III. SATURATION EVOLUTION WITH FLOW RATE AND HISTORY

Figure 2 represents the residual saturation $S$ of the $nw$ fluid at steady state conditions versus the $w$-phase flow rate, i.e., the capillary number Ca. Each point corresponds to both a constant measured pressure drop and a constant $nw$ phase saturation. Each curve, uniquely marked by different symbols, corresponds to a desaturation experiment set, where the flow rate is progressively increased starting from the lowest capillary number value $\text{Ca}_{\text{min}} \simeq 3.7 \times 10^{-7}$. The initial saturation $S_{\text{init}}$ is also reported on the left side of the vertical axis. As expected, increasing the $w$ fluid flow rate results in a decrease of the $nw$ saturation in all the series. As viscous forces become progressively more important at the blob interfaces, it results in the mobilization and the sweeping of several blobs. When a new steady state configuration is established, the $nw$-phase residual saturation consists of immobile blobs only.

In Fig. 2, we distinguish two types of behaviors. By example, full (red) left-pointing triangles and full black squares exhibit a *plateau* at low Ca in continuation from $S_{\text{init}}$. The other ones drop down from the initial saturation $S_{\text{init}}$ to a smaller $S$ value at $\text{Ca}_{\text{min}}$. The latter behavior corresponds to the larger initial saturation, $S_{\text{init}} \gtrsim 0.55$.

Intuitively, one would have expected that all series exhibit a *plateau* as sketched in the inset of Fig. 2: at very low Ca, the pressure field generated by the flow is not able to move any $nw$ blobs, the $nw$ saturation remains constant. This requires that the initial wetting phase is percolating, where flow is allowed without moving the other phase. One should then be able to find a small enough Ca without modifying the initial saturation.

We identified two reasons why some series does not display a *plateau*. On one hand, if the wetting fluid is not initially percolating, a small increase of Ca induces an imbibition front which sweeps a significant amount of nonwetting phase. On the other hand, even if the initial state is percolating, the experimental $\text{Ca}_{\text{min}}$ might be already too large and thus mobilize some blobs. It is thus not surprising that the most important saturation drops correspond to high initial saturation, where the probability of having a percolating wetting phase is smaller.

At low Ca numbers, the saturation path depends then on the initial conditions. Interestingly, at large capillary numbers $\text{Ca} \gtrsim 10^{-5}$, the data series tend to collapse to a single master curve, meaning that the saturation does not depend any more on the initial configuration and the flow history. Consequently, the saturation is only a function of $\text{Ca}_M$. This could then imply that a $nw$-phase rearrangement had occurred, leading to analogous phase distribution patterns above that capillary number.

To enlighten this point, we plot in Fig. 3 the local mean saturation of the $nw$ phase at steady state *averaged over all realizations* with the same capillary number *but* with different initial conditions. A local average saturation equal to 1 (shown in white color) denotes a location where the $nw$ fluid is persistently present in all realizations. On another hand, a zero probability (shown in black color) indicates a location where $nw$ is practically never present. At initial states [Fig. 3(i)], an almost spatially uniform probability coverage is observed, with the exception of the locations occupied by the solid obstacles, where the probability is always equal to 0 (black color). This indicates the possibility of encountering one or the other phase at any location. However, as Ca increases, we observe a clear enhancement of the contrast which illustrates the fact that phase distribution patterns become more and more deterministic. Namely, there are clear locations where the probability over all series is equal to 1, and others where it is equal to 0. It is also important to note that the locations of probability 1 at high capillary numbers [e.g., in Fig. 3(d)] are already present at low Ca [e.g., in Fig. 3(a)]. This indicates that a significant part of the saturation remains unmoved during the entire desaturation process: around 90% of blobs present at the

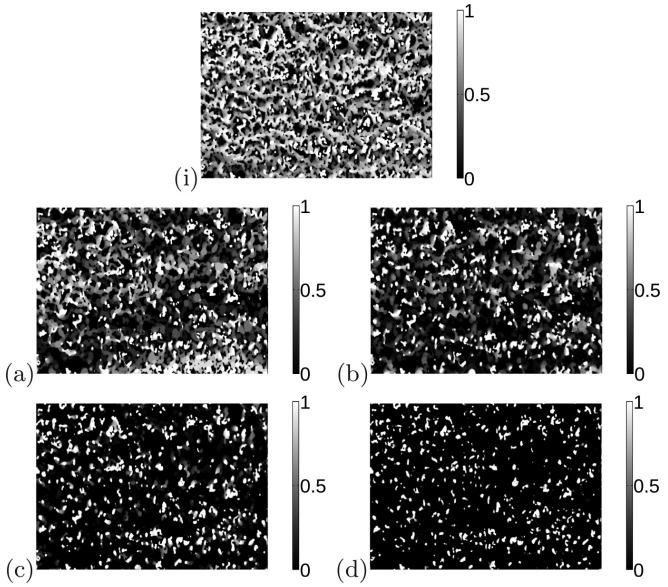


FIG. 3. Mean correlation maps between all experiments at initial conditions (i) and at different capillary numbers: Ca $= 3.7 \times 10^{-7}$ (a), $7.4 \times 10^{-6}$ (b), $3.0 \times 10^{-5}$ (c), and $3.3 \times 10^{-4}$ (d).

highest capillary number are also present at any Ca. We denote as $S_0$ this irreducible residual saturation.

To capture in more details the effects of Ca on $S$, we show in Fig. 4 a log-log plot of $S - S_0$ versus the capillary number, where $S_0 \sim 0.09$. For Ca $\gtrsim 10^{-5}$, all desaturation experiments collapse to a single curve scaling as

$$S - S_0 \propto \mathrm{Ca}_M^{-0.52 \pm 0.05}. \quad (1)$$

This scaling can be interpreted in the light of the numerical work of Knudsen and Hansen [24] in a pore network model. Starting from a given randomly distributed saturation, they increased the Ca number in order to determine the transition from single to two phase flow. This transition curve should be comparable to our $S$(Ca) curve. Indeed, the onset of two-phase flow requires few $nw$-phase mobilization which will be swept out of our system, leading to desaturation. However, as we have shown, this transition might not be relevant at low Ca number since the flow history and the initial saturation strongly

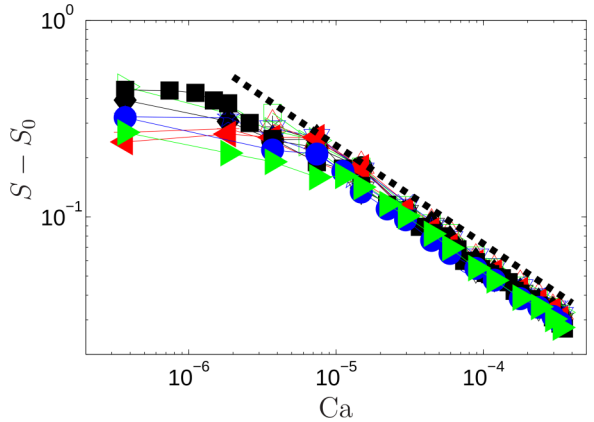


FIG. 4. (Color online) Log-log plot of $S - S_0$ as a function of Ca with $S_0 = 0.09$. The dotted line corresponds to $\mathrm{Ca}^{-1/2}$.

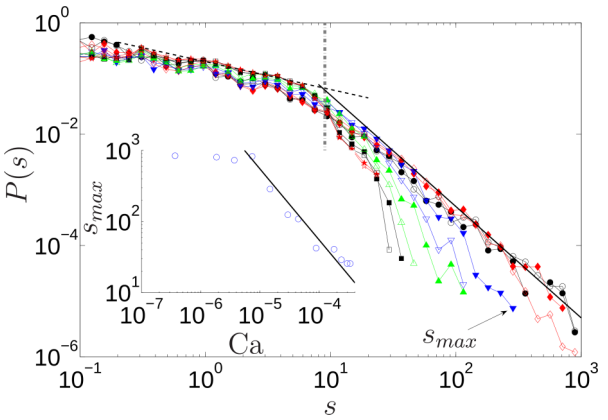


FIG. 5. (Color online) Probability distribution function $P(s)$ of $nw$ blobs of area $s$ at steady state for all experiments from Ca $= 3.7 \times 10^{-7}$ to $3.7 \times 10^{-4}$. Black lines are power law, $P(s) \propto s^{-1/2}$ (dotted line) and $P(s) \propto s^{-2}$ (continuous line). The transition between those power laws, at the size $s_c$, is represented by a vertical grey dashed line. The Ca dependance of the cutoff size $s_{\max}$ is shown in the inset where the line is $s_{\max} \propto \mathrm{Ca}^{-1}$. The blob area unit is mm$^2$.

influence the transition. The two curves are then comparable only at high capillary numbers or low saturation. Despite the fact that they empirically proposed an exponential law Ca $\propto e^{-\alpha S}$, we note that our power law could equivalently match their numerical points.

*Nonwetting blob size distribution.* Of significant interest in our analysis is the probability distribution function (PDF) $P(s)$ of blob sizes $s$ at steady state conditions. Our experimental layout and the high resolution of the pictures (1 pixel $= 2.7 \times 10^{-3}$ mm$^2$) allow for covering an extensive range of blob sizes, ranging from two orders of magnitude *smaller* than the typical pore size (order $s_c \sim 10$ mm$^2$) up to two orders of magnitude larger. Figure 5 shows the corresponding blob size distribution averaged over all realizations at fixed Ca values.

Several important scaling behaviors are observed in Fig. 5. For blob sizes smaller than $s_c$, the PDF decreases smoothly with the same trend for all Ca values. If we were to fit these data with a power law, it would follow quite reasonably a decay $P(s) \propto s^{-1/2}$. This distribution may correspond then to the residual saturation $S_0$ of nonwetting blob which is noticeably smaller than $s_c$. For blob sizes larger than $s_c$, the PDF depends strongly on the Ca value. Increasing Ca from the lowest value (Ca $= 3.7 \times 10^{-7}$), the data series depart from the power law scaling, $P(s) \sim s^{-1.95 \pm 0.1}$, exhibiting a large size cutoff $s_{\max}$. After determining the cutoff area $s_{\max}$ as being the largest observed blob, we plot its evolution with Ca in the inset of Fig. 5. It can be seen that $s_{\max}$ decreases with Ca following a scaling law:

$$s_{\max} \propto \mathrm{Ca}^{-1.1 \pm 0.1}. \quad (2)$$

We note, however, that $s_{\max}$ displays an upper bound which is rather large (equivalent diameter $\sqrt{900\ \mathrm{mm}^2} \simeq 3$ cm) and this may be attributed to the finite size of our sample. This upper bound is reached for capillary number around Ca $\simeq 10^{-5}$, which is comparable to the value at which the saturation $S$ starts to become independent of the initial saturation (Fig. 4).

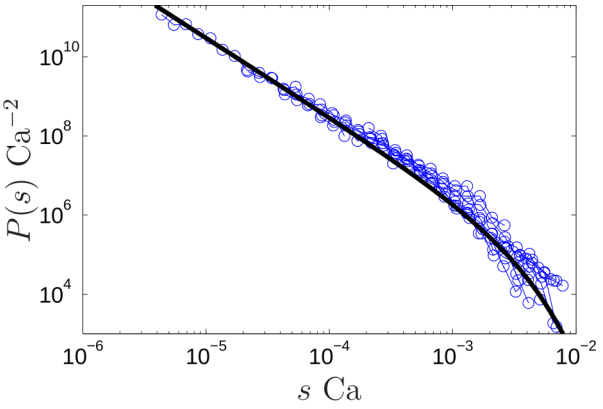


FIG. 6. (Color online) Scaling relation defined by Eq. (3) for blobs larger than $s_c$, $P(s)\mathrm{Ca}^{-2}$ versus $\hat{s} = s\mathrm{Ca}$. The continuous line is proportional to $\hat{s}^{-2}\exp(-\hat{s})$.

By analogy with critical behavior (e.g., percolation theory [25]), we can propose the following scaling function:

$$P(s) \propto \mathrm{Ca}^2 f(\mathrm{Ca}s) \quad \text{with} \quad f(x) = x^{-2}e^{-x}, \qquad (3)$$

according to Eq. (2). This renormalization is tested with our data for $s > s_c$ in Fig. 6 showing a rather good collapse for all the data series. Moreover, the above proposed scaling function is also validated by this figure (continuous black curve).

The scaling expressions of Eqs. (2) and (3) are similar to the ones observed in [16,17], in which the cluster size distribution was found to scale as $P(s) \propto s^{-\tau}e^{-s/s_{\max}}$ with $s_{\max} \propto \mathrm{Ca}^{-\zeta}$. Their fit to the data led to $\zeta \simeq 0.98 \pm 0.07$ and $\tau = 2.07 \pm 0.18$. The latter is reminiscent to the corresponding percolation exponent. The exponents measured in our study ($\zeta = 1.1 \pm 0.1$ and $\tau = 1.95 \pm 0.1$) are interestingly very close to the above values, despite the significant differences in the experimental setups between the two studies. Indeed, in Refs. [16,23] the fluids are a liquid and air (negligible viscosity compared to the liquid) which flow simultaneously (co-injection) in the quasi -two-dimensional glass beads porous medium. Moreover, the measured air blob size distributions include both mobile and immobile blobs, that could follow different distributions as shown in numerical simulations [22]. Additionally, Aursjo *et al.* [20] have recently showed the strong deviation of those coefficients by replacing the air by a viscous liquid in the same system as [16,23]. The reported exponents, $\tau$ ranging from 1.32 to 1.48 and $\zeta$ from 0.89 to 0.51, depend on the flow rate ratio of the two simultaneously injected liquids and are definitively smaller than their previous air-liquid ones. Besides, in the three-dimensional (3D) packed beads experiments of [18], while the cutoff was not really scaling as Eq. (2), the PDF of the linear extension of the blobs was compared to 3D percolation theory. Therefore, this supports the contention that the exponent $\tau = 2$ accounting for our data of wetting fluid flowing across a porous medium with immobile nonwetting blobs is consistent with 2D percolation.

## IV. FLOW REGIMES

As discussed earlier, the permeability of our experimental domain is significantly lower than the permeability of a Hele-Shaw cell of the same thickness. This is due to the presence of the engraved solid obstacles that modify the flow stream. We thus expect that the presence of immobile $nw$ phase blobs has also a profound impact on the "effective" permeability of the medium, as experienced by the flowing $w$ phase. To address this issue, we measure the pressure drop along the medium versus the imposed $w$ phase flow rate. The effective permeability of the medium is then defined as $K_{eff} = k\,k_r = e^2\mathrm{Ca}/B$, where $k$ is the intrinsic medium permeability and $k_r < 1$ is the relative permeability for the $w$ phase.

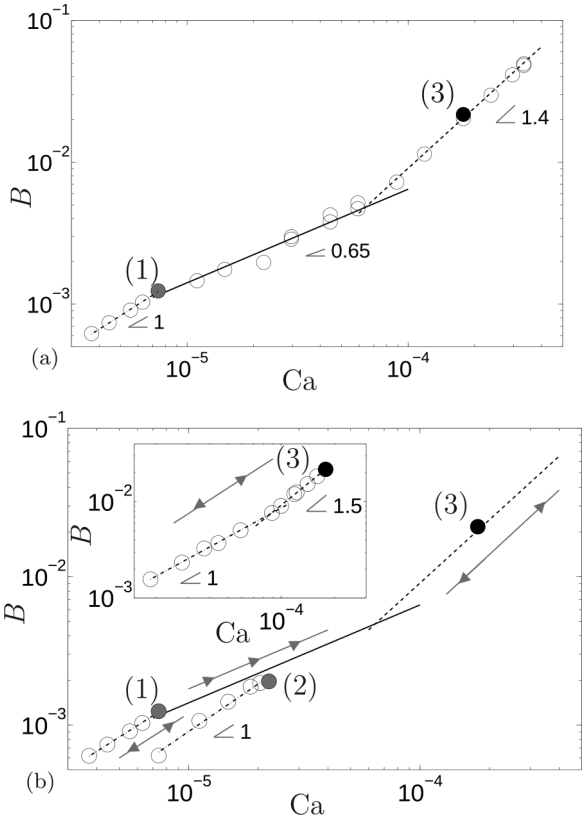


FIG. 7. Nondimensional pressure drop $B$ vs nondimensional flow rate Ca at steady state. The lines through the data are guide lines with their corresponding slopes. (a) Data corresponding to an increase Ca from its lowest value. (b) Illustration of the hysteresis-history effect. The plot is identical but with including three Ca decrease from $\mathrm{Ca}_M$ (1, 2, 3). The double arrows indicates a reversible process with respect to Ca whereas the one way arrows indicates an irreversible one. For sake of clarity, we have plotted the decrease from $\mathrm{Ca}_{(3)}$ (full black circle) as inset.

Figure 7 displays the nondimensional pressure drop $B$ versus the nondimensional wetting flow rate Ca. The top figure corresponds to an *increase* of Ca according to the experimental procedure described in the previous sections. Three different flow regimes can be clearly identified in this figure:

(i) At low Ca values, the pressure drop is linear with the flow rate (slope ~1).

(ii) At intermediate Ca values and over one order of magnitude, the slope is significantly smaller, around $0.65 \pm 0.1$.

(iii) For larger Ca values, the slope increases again to a value larger than 1, around $1.4 \pm 0.1$.

To account for these different regimes, we need to compare with the saturation evolution. The low capillary number regime corresponds to the situation where the immobile $nw$-phase saturation remains constant, that is on the saturation *plateau* in Fig. 2. Therefore the observed linear dependence of the pressure drop with Ca is a classical Darcy's law for the continuous $w$ phase through a medium of solid obstacles and immobile blobs. It is worth noting that this regime is "reversible" with respect to an increase or decrease of the flow rate.

In the intermediate regime, as the capillary number increases, part of the $nw$ phase is mobilized and swept by the flowing $w$ phase, leading to a continuous decrease in residual $nw$ saturation (see Fig. 2). Therefore the increase of pressure drop results from two competing effects. On one hand, the pressure loss increases with the flow rate, but on the other hand the increase of number of flow paths results in a decrease of the hydraulic resistance. The resulting slope of the curves is then smaller than 1 ($0.65 \pm 0.1$). Such non-Darcy flow regimes have also been reported in the literature without the other regimes, but with somehow different coefficients ($0.54 \pm 0.08$ in Ref. [17] and $0.35 \pm 0.08$ in Ref. [26]). From a theoretical model, Sinha and Hansen [21], based on an analogy with yield stress fluid in porous media [27,28], obtained a coefficient $1/2$. As the extension of the intermediate regime is rather small, we can barely conclude that the exponent we get is consistent with the theoretical one.

We note that the desaturation process during this intermediate regime is "irreversible," namely, decreasing the flow rate leads to a different slope $\sim$1 (see bottom of Fig. 7). It is also very interesting to note the larger than 1 slope (1.4) in the case of $\mathrm{Ca} > 10^{-4}$ values, despite the fact that the residual saturation remains practically unchanged in this region. We would have thus expected a constant effective permeability and a Darcy-type dependance between the flow rate and the pressure drop. This effect should be attributed to the onset of inertial forces, as also discussed earlier, since the corresponding Reynolds number is of the order of $\mathrm{Re} \sim 5$. To test this conjecture, we have plotted (inset, bottom of Fig. 7) the pressure drop versus Ca but *decreasing* the flow rate from the black full circle. The slope first remains of the same order ($\sim$1.5) and below $\mathrm{Ca} \sim 10^{-4}$ tends to 1. Therefore, the slope change corresponds to the inertial correction from a linear Darcy regime to the "so-called" Forchheimer [1] one. We also note that this process is reversible.

To sum up, Fig. 8 gives a schematic of the "ideal" history effect on the relation between pressure drop ($B$) versus flow rate (Ca) in the case of creeping flow, $\mathrm{Re} \ll 1$ and thus negligible inertial effects.

For each point on the increasing Ca curve [Fig. 7(a)], we can measure the relative permeability directly from the slope 1 regime or by decreasing Ca enough to fall into a slope 1 regime, to avoid any Forchheimer effects.

In Fig. 9, we have plotted the measured permeability, normalized by the porous medium permeability without blobs ($k \sim 2 \times 10^{-9}$ m$^2$), $k_r$, the relative permeability, along with the saturation evolution ($S$, Fig. 2). This figure summarizes the main features described above getting rid of the inertia effect. At low and high Ca regimes, the permeability is constant. In the intermediate regime, the increase of flow rate induces an irreversible increase of the permeability associated to a decrease of saturation which saturates at a larger value (twice the low Ca one) at large Ca.

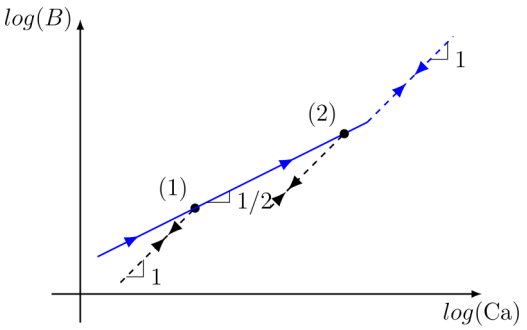


FIG. 8. (Color online) Sketch of the history of the different flow regimes without non-linear effect (see text). (1) and (2) refer to two $\mathrm{Ca}_M$ below which the variation of the capillary number is reversible. The arrows (double or single) correspond respectively to reversible (dashed line) and irreversible regimes (continuous blue line).

## V. FINAL DISCUSSION AND CONCLUSION

We have investigated experimentally the displacement of a nonwetting fluid by a wetting one in a quasi-two-dimensional porous media. Since, blobs fragmentation and/or mobilization require a minimum amount of stress, the decrease of $nw$ saturation of the medium is an irreversible process. An increase of flow rate might then desaturate the media whereas a decrease is enabled to change the blob configuration. Thus, the $nw$ saturation depends necessarily on the flow history and more specifically on the highest capillary number reached in the past, noted $\mathrm{Ca}_M$. Depending on this maximal value, we have observed two different behaviors. At low $\mathrm{Ca}_M$, the final saturation significantly depends on the initial configuration. However, for large $\mathrm{Ca}_M$, the saturation is independent of the flow history. Moreover, the evolution of the saturation with $\mathrm{Ca}_M$ follows a power-law scaling towards an asymptotic as $S - S_0 \propto (\mathrm{Ca}_M)^{-1/2}$. The physical reason behind this observation

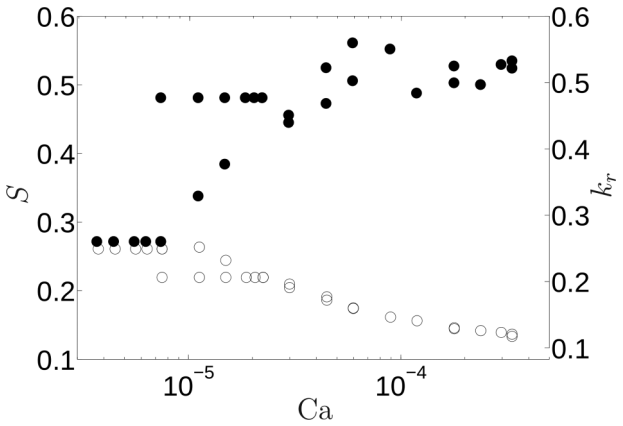


FIG. 9. Relative permeability (full symbol) and saturation (empty symbol) as a function of capillary number. The permeability is normalized with $k$, the single phase one.

is the existence of an irreducible residual nonwetting fluid, that cannot be removed from one realization to the other.

The blob size distribution was measured over four orders of magnitude. For blob sizes smaller than the typical pore size, the PDF decrease can be reasonably described with a power law $P(s) \propto s^{-1/2}$. For larger sizes, the PDF follows another power law $P(s) \propto s^{-2}$, with a cutoff at large sizes, $s_{\max} \propto \mathrm{Ca}^{-1}$.

Three different flow regimes have been clearly identified. At low Ca, the flow rate is linear with the applied pressure drop: the flow takes place in the preexisting percolating paths but it is not large enough to mobilize the nonwetting fluid. This regime is reversible but it depends strongly on the initial conditions. At intermediate flow rate, the viscous drag becomes sufficient to start moving some immobile fluids and creating new flow paths. This regime is irreversible, and thus depends on $\mathrm{Ca}_M$. The dependence seems to follow also a power law: $B \propto \mathrm{Ca}_M^{0.65}$ which might be understood from an analogy with yield stress fluid in porous media. For larger Ca, we should expect to recover a linear regime. However, due to inertial effects, we observed a nonlinear power law $B \propto \mathrm{Ca}^{1.4}$.

It is worth noting that thanks to our rather wide range of Ca values we have been able to observe these three flow regimes and to depict in more detail the intermediate one. Using our extrapolation procedure we have been able to determine the history of the relative permeability with the capillary number.

In the present work we have used a particular 2D porous medium which requires a porosity higher than 0.5 to percolate. An interesting extension of this work could be to investigate different types of media.

It would be interesting to pursue this work to investigate the implications of those results to simultaneous two phase flow experiments. In particular, if one distinguishes the mobile and immobile fluid, one could idealize the problem by conjecturing that the immobile part is distributed similarly as in the present paper whereas the mobile $nw$ blobs flow only inside the opened channels. One could then expect that the relative permeabilities present similar properties as in this work (irreversibility, strong dependence to the initial configuration at low Ca, etc). Moreover, this picture could be more complicated as in the permanent regime, the immobile blobs can become mobile, and vice versa as discussed in [22].

## ACKNOWLEDGMENTS

The authors would like to thank Prof. A. Hansen for useful discussions, and the Agence Nationale de la Recherche for financial support of the project LaboCothep ANR-12-MONU-0011.

[1] F. A. Dullien, *Porous Media: Fluid Transport and Pore Structure* (Academic, New York, 1991).
[2] D. G. Avraam and A. C. Payatakes, J. Fluid Mech. **293**, 207 (1995).
[3] A. C. Payatakes, K. M. Ng, and R. W. Flumerfelt, AIChE J. **26**, 430 (1980).
[4] M. M. Dias and A. C. Payatakes, J. Fluid Mech. **164**, 305 (1986).
[5] M. M. Dias and A. C. Payatakes, J. Fluid Mech. **164**, 337 (1986).
[6] D. Avraam and A. Payatakes, Trans. Porous Media **20**, 135 (1995).
[7] O. I. Frette, K. J. Måløy, J. Schmittbuhl, and A. Hansen, Phys. Rev. E **55**, 2969 (1997).
[8] P. Amili and Y. Yortsos, Trans. Porous Media **64**, 25 (2006).
[9] S. E. Powers, L. M. Abriola, and W. J. Weber, Water Resour. Res. **28**, 2691 (1992).
[10] M. Valavanides and A. Payatakes, Adv. Water. Resour. **24**, 385 (2001).
[11] R. Lenormand, C. Zarcone, and A. Sarr, J. Fluid Mech. **135**, 337 (1983).
[12] W. L. Olbricht and L. G. Leal, J. Fluid Mech. **134**, 329 (1983).
[13] I. Chatzis and F. Dullien, J. Colloid Interface Sci. **91**, 199 (1983).
[14] O. Vizika, D. Avraam, and A. Payatakes, J. Colloid Interface Sci. **165**, 386 (1994).
[15] W. L. Olbricht, Annu. Rev. Fluid Mech. **28**, 187 (1996).
[16] K. T. Tallakstad, G. Løvoll, H. A. Knudsen, T. Ramstad, E. G. Flekkøy, and K. J. Måløy, Phys. Rev. E **80**, 036308 (2009).
[17] K. T. Tallakstad, H. A. Knudsen, T. Ramstad, G. Løvoll, K. J. Måløy, R. Toussaint, and E. G. Flekkøy, Phys. Rev. Lett. **102**, 074502 (2009).
[18] S. S. Datta, J.-B. Dupin, and D. A. Weitz, Phys. Fluids **26**, 062004 (2014).
[19] S. S. Datta, T. S. Ramakrishnan, and D. A. Weitz, Phys. Fluids **26**, 022002 (2014).
[20] O. Aursjø, M. Erpelding, K. T. Tallakstad, E. G. Flekkøy, A. Hansen, and K. J. Måløy, Front. Phys. **2**, 63 (2014).
[21] S. Sinha and A. Hansen, Europhys. Lett. **99**, 44004 (2012).
[22] A. G. Yiotis, L. Talon, and D. Salin, Phys. Rev. E **87**, 033001 (2013).
[23] G. Wagner, A. Birovljev, P. Meakin, J. Feder, and T. Jøssang, Phys. Rev. E **55**, 7015 (1997).
[24] H. A. Knudsen and A. Hansen, Eur. Phys. J. B **49**, 109 (2006).
[25] D. Stauffer and A. Aharony, *Introduction to Percolation Theory* (Taylor and Francis, London, 1991).
[26] E. M. Rassi, S. L. Codd, and J. D. Seymour, New J. Phys. **13**, 015007 (2011).
[27] L. Talon and D. Bauer, Eur. Phys. J. E **36**, 1 (2013).
[28] T. Chevalier and L. Talon, Phys. Rev. E **91**, 023011 (2015).